RSC Advances

PAPER

View Article Online
View Journal | View Issue

Cite this: *RSC Adv.*, 2017, **7**, 39859

A tunable volatile organic compound sensor by using PtO_x/GQDs/TiO_2 nanocomposite thin films at room temperature under visible-light activation†

Shaofeng Shao, *[a] Yunyun Chen,[a] Shenbei Huang,[a] Fan Jiang,[a] Yunfei Wang[a] and Ralf Koehn[b]

Received 7th July 2017
Accepted 9th August 2017

DOI: 10.1039/c7ra07478f

rsc.li/rsc-advances

In this work, a PtO_x/GQDs/TiO_2 nanoporous thin film with high sensitivity and excellent selectivity at room temperature is fabricated *in situ* on a sensor device by using an oxygen-plasma treatment. PtO_x/GQDs/TiO_2 nanocomposite thin films exhibit distinctly different sensor responses toward oxygen-functionalized VOCs under visible-light activation. In particular, the PtO_x/GQDs/TiO_2 nanocomposite thin films depict a reversible change in their sensing behaviour from p-type to n-type for oxygen-functionalized VOCs as a function of the oxygen-plasma treatment, while these gas sensors present p-type sensing performance for aromatic VOCs throughout. Furthermore, the gas sensors in this work exhibit high sensitivity to isopropanol gas with a response value of up to 4.4 to 1 ppm and a short response time of 9 seconds at room temperature. The reported synthesis procedure to fabricate a tunable and sensitive VOC sensor may be extended to a potential real-world application in breath diagnosis.

1. Introduction

Early breath diagnosis of lung cancer is significant for enabling effective treatment and for improving the survival rates of patients. To enhance the accuracy of breath diagnosis, it is crucial to develop breath analysis tools that can efficiently detect specific volatile organic compounds (VOCs).[1,2] Recently, highly efficient VOC gas sensors based on nanoporous sensing materials have attracted considerable interest because their ordered nanostructure could provide a large specific surface area and abundant accessible pores, which could facilitate the effective adsorption and diffusion of the target gas molecules over the entire material surface. Studies have also shown that much less hindrance is found in the electron-transport process for TiO_2 based ordered nanoporous structures, leading to higher sensor sensitivity and a lower operation temperature.[3–7] However, most of the sensors based on porous TiO_2 sensing materials operate at a temperature over 200 °C which increases energy consumption and the cost of the sensors.[8,9] For reducing the operation temperature, some techniques have been applied, such as doping the TiO_2 with additives,[10,11] and illuminating the sensors with UV radiation. Among these techniques, UV light irradiation has attracted increasing attention as a promising strategy to achieve room temperature response.[12,13] Despite a lot of efforts having been made, the applications of UV-light-activated sensors in practice remain many challenges. Chen *et al.* reported that sensing response of porous TiO_2 film was fast typically reaching 95% of the maximum within 30 s, but recovery was slower, typically 5 min to achieve full recovery for injections at sub-ppm levels.[14] Aluri *et al.* also found that Pt–TiO_2 nanoclusters were able to obtain response to sub-ppm level concentration of analytes, however, the sensitivity was still low.[3] In addition, a UV light source is expensive and UV rays are harmful to human health, resulting in increasing cost and restricting its real-world applications in the gas sensing region. Zhai *et al.* considered that the use of solar energy as the operating source was the optimal choice to reduce its cost as well as avoiding UV exposure of the human body.[15] Therefore, it is necessary to fabricate a novel gas sensing material with narrow band gap, and enhance the gas sensing performance to sub-ppm level VOCs gas under visible light activation.

To obtain the TiO_2 based gas sensing material with narrow band gap, various routes such as doping with noble metal elements,[16,17] and coupling with narrow-band gap materials[18–20] were employed. Recently, graphene quantum dots have become an active area of great interest in detection of VOCs gas because of large surface areas and unique electronic properties.[21,22] Besides, Pan *et al.* reported that the electronic structure of GQDs was tunable in a wide energy range by changing size,[23] which was highly necessary for achieving selectivity for various target applications. Furthermore, the observation of Wang *et al.* confirmed that quantum confinement feature of GQDs made it

[a]*Jiangsu Key Laboratory for Optoelectronic Detection of Atmosphere and Ocean, Nanjing University of Information Science & Technology, Nanjing, China. E-mail: ssfshao@nuist.edu.cn; Fax: +86-025-58731031; Tel: +86-025-58731031*

[b]*Center for Free-Electron Laser Science, Building 99, Notkestrasse 85, Hanburg, Germany*

† Electronic supplementary information (ESI) available. See DOI: 10.1039/c7ra07478f

possible to obtain narrow bandgap by modifying the size of GQDs.[24] For breath analysis, many trace VOCs are detected in human breath at concentration from ppm to ppt level. Our previous work reported that Pt/GQDs/SnO_2 thin film presented tunable transition of sensing behavior from p-type to n-type to acetone gas at room temperature, but showed weak response to sub-ppm level VOCs. So it is necessary for gas sensor to detect sub-ppm level VOCs gas with high sensitivity at room temperature. Up to now, there are few reports on GQDs/TiO_2 based gas sensors with illumination of visible light activation for detecting sub-ppm level VOCs gas.

In this work, we report the fabrication of a new type of ordered nanoporous TiO_2 thin film supporting both PtO_x nanoparticles and GQDs. The size and oxygenated species of GQDs are modified by oxygen-plasma treatment to control the TiO_2-support interactions. After the oxygen-plasma treatment, the GQDs in the thin film still retain the sp^2 hybridized graphite network with excellent conductivity and stability of the graphene structure. Interestingly, the ordered nanoporous PtO_x/GQDs/TiO_2 thin film displays high sensitivity (down to 0.1 ppm) and selectivity toward representative VOCs groups (benzene, toluene, isopropanol, ethanol, butanol, acetone, and aether) under illumination of visible light at room temperature. Even more interesting is the fact that the sensing behaviors are significantly different, depending on the surface state of the nanocomposite thin film and the type of VOCs. In particular, the PtO_x/GQDs/TiO_2 nanocomposite thin films present reversible change of sensing behaviour from p-type to n-type sensing behaviour for oxygen-functionalized VOCs as function of oxygen-plasma treatment, while these gas sensors present p-type sensing performance for aromatic VOCs throughout. Such difference in sensing behaviours toward different kinds of VOCs gas might originate from the modified functionality of the PtO_x/GQDs/TiO_2 thin film, which plays a key role in interacting with VOCs and causes changes in the bandgap.

2. Experimental section

2.1 Fabrication of GQDs

GQDs have fabricated from GO quantum dots by using a facile one-step hydrothermal method.[25,26] In a typical synthesis, 100 mg GO quantum dots (XFNANO) and 10 ml 30% hydrazine hydrate aqueous solution were suspended in deionized water (40 ml) with the aid of ultrasound (120 W, 40 kHz) for 15 min, and then the suspension was transferred to a Teflon-lined autoclave and heated up to 180 °C for 8 h. After naturally cooling to room temperature, the mixture was filtrated using a 0.22 μm microporous membrane and the brown filtrate then centrifuged at high speed to obtain GQDs (15 000 rpm, 20 min).

2.2 Ordered nanoporous PtO_x/GQDs/TiO_2 thin films fabrication and characterization

PtO_x/GQDs/TiO_2 sensing thin film was fabricated through a simple route. The Ti precursor solutions were prepared by dissolving 0.15 g $TiCl_4$ (Aldrich) in 0.04 mol isopropanol in the presence of 5×10^{-6} mol PluronicF127 triblock copolymer (Sigma). 4 mg GQDs, 2.5 mg $PtCl_4$ (Aldrich) and 20 μl 2 M citric acids were added in 400 μl deionized water, respectively, and then dropped in 80 μl 12 M HCl with the aid of ultrasound for 5 minutes, then mixed with the above Ti precursor solution under constant stirring for overnight. The resulting (clear) PtO_x/GQDs–Ti precursor solution was stable over two weeks period. Gas sensing films were synthesized by spin-coating 40 μl of the PtO_x/GQDs–Ti precursor solution on one sensor device of *ca.* 10×10 mm^2 with interdigital electrode at 4000 rpm for 60 seconds under 30% relative humidity, and then dried at 60 °C for one hour. The structures of the interdigital electrode were described in our previous work. The films exposed to a water vapor hydrothermal treatment, 95% relative humidity, at 120 °C for 48 h. The relative humidity achieved using a supersaturated salt aqueous solution, kept at 120 °C, in the humidity controllable chamber. The nanocomposite thin films were then oxygen-plasma treated (Femto, 40 kHz, 100 W) for 1 minute (sample PGT-PS-E1), 2 minutes (sample PGT-PS-E2), 3 minutes (sample PGT-PS-E3) and 4 minutes (sample PGT-PS-E4), respectively.

2.3 Gas-sensing measurement

The gas sensing properties are determined in a sample cell consists of a sample chamber and has a gas inlet and outlet. A certain concentration of VOCs gas or pure air is periodically passed into the test chamber based on computer-controlled mass flow controllers (MFCs), and the total flow rate is maintained at 500 sccm. During the measurements 460 nm monochromatic light as the excitation light source is irradiated on the sensor through the quartz window. On a controlled irradiation measurement, the light irradiation is turned on after the sensor was put into the test chamber with analyte. After the resistance keeps stable, the irradiation is turned off and the sensor is taken out to recover in pure air. Resistance changes upon sample exposure to gases are recorded by a high resistance meter Keithley 6517B. The sensor response is defined as $(R_a - R_g)/R_g$ or $=(R_a - R_g)/R_a$, where R_a and R_g are the sensor resistances in air and in the target gas, respectively. This parameter is positive (negative) for n-type (p-type) sensing behavior. Here, the response or recovery time defined as the time taken for the sensor to achieve 90% of its maximum response or decreases to 10% of its maximum response, respectively.

2.4 Characterization

SAXRD patterns of the thin films were taken on an XDS-2000 diffractometer (Scintag Inc.) using Cu K radiation. WAXRD data were obtained by a Bruker D8 Advance X-ray diffractometer with Cu Ka (0.15406 nm) radiation. Field-emission scanning electron microscopy (FE-SEM, Hitachi S-4800) was used to observe the morphologies of the sensing films. Nitrogen sorption measurements were carried out at 77 K using a NOVA 4000e (Quantachrome Instruments) on nanocomposite scratched from several films. High resolution transmission electron microscopy (HRTEM) was performed using a FEI Titan 80-300 equipped with a field emission gun operated at 300 kV; film

parts were scratched from the substrate and collected on an amorphous holey carbon film on a copper grid. Photoluminescence (PL) emission spectra were controlled on a FL3-221 fluorescence spectrophotometer (Jobin Yvon, λ_{ex} = 365 nm) at room temperature. XPS spectra were recorded using a Kratos Axis Ultra DLD spectrometer employing a monochromated Al-Ka X-ray source ($h\nu$ = 1486.6 eV), hybrid (magnetic/electrostatic) optics and a multi-channel plate and delay line detector (DLD). Surface charging was corrected by referencing the spectra to C–C state of the C 1s peak at binding energy at 284.6 eV. All XPS spectra were recorded using an aperture slot of 300 × 700 microns, survey spectra were recorded with a pass energy of 160 eV, and high resolution spectra with a pass energy of 40 eV.

3. Results and discussion

3.1 Material properties

The research aim in this work is to find the influence of oxygen-plasma treatment on the nanostructured ordering, bandgap, and gas sensing behaviour of nanocomposite PtO_x/GQDs/TiO_2 porous thin films. For this purpose, four nanoporous PtO_x/GQDs/TiO_2 thin films are synthesized by water vapor hydrothermal treatment and then being treated by oxygen-plasma treatment for different time at low temperature. The structure ordering of the four treated thin films are examined by small angle X-ray diffraction. Generally, for the as-synthesized air-dried PtO_x/GQDs–Ti hybrid thin film synthesized from the precursor solution with only HCl, no diffraction peaks were observed within the SAXRD patterns (not shown for brevity). It is attributed to the factor that the acidity of the whole system added with HCl in evaporation process reduces quickly and thus consequently influences the hydrolysis behavior of titanium species and the self-assembly process. In this work, when citric acids are added, they serve on sustained-release agents to sustain an acidic equilibrium environment for precursors. At the start, their influence is not obvious, but at the end of the evaporation process this influence develops into more significant as hydro-carboxylic acids' concentration increase in the spin-coated thin film. Yuan *et al.* assumed that volatilization behavior of the acids is an important factor for obtaining the ordered nanostructure of sensing films.[27] As for our synthesis, the precursor solutions are relatively dilute, and the inorganic polymerization can be readily dominated by an acid, which is subsequently removed by evaporation. After evaporation process, the as-synthesized composite thin film shows a diffraction peak in SAXRD pattern, as shown in Fig. 1. However, for the as-synthesized pristine TiO_2 film, no diffraction peaks is observed within the SAXRD pattern, indicating a disordered nanostructure.

The SAXRD patterns (Fig. 1) of thin films from psHT treated film to PGT-PS-E3 depict a significant increase in intensity of the diffraction peak, indicating an increase in the nanostructure ordering with the plasma treatment. It has to be noted that these films undergo the plasma treatment to remove the template. It means that, during the film being treated in the oxygen atmosphere, oxidation reaction between the template and the TiO_2 nanoparticle has taken place, which modifies the nanopores. Robben *et al.* reported[28] it is conceivable that the template induces chemical reaction in the outer surface areas of TiO_2 nanoparticles under the influence of the oxygen atmosphere and that these reactions can proceed fully into the grains, thus leading to uniform nanopore size after the plasma treatment. Liu *et al.* reported that the incorporation of the carbon into the TiO_2 based nanomaterials can effectively influence the nanostructure stability of nanocomposite film.[29] For sample PGT-PS-E4 with further oxygen-plasma treatment, the intensity of the peak decreases gradually with the further removal of carbon from the thin film. However, the calculated cell parameters are not significantly changed, indicating that the nanostructure is stable and the shrinkage not obviously occurs.

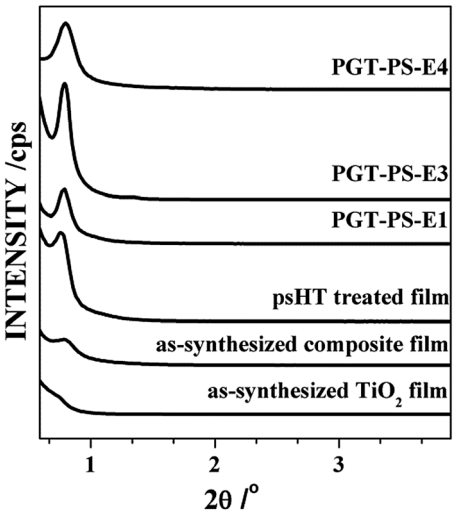

Fig. 1 Small-angle XRD patterns of as-synthesized PtO_x/GQDs–Ti film, psHT treated film PtO_x/GQDs/TiO_2 film, PGT-PS-E1, PGT-PS-E3, and PGT-PS-E4.

Fig. 2 shows the wide-angle XRD patterns of the PGT-PS-E1 and PGT-PS-E3 scratched films. Both scratched films exhibit distinct peaks contributed by TiO_2 (JCPDF 21-1272). The XRD pattern of PGT-PS-E1 thin film exhibits six discrete *hkl* reflection

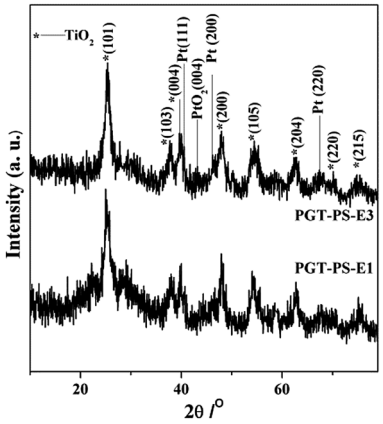

Fig. 2 WAXRD patterns of PGT-PS-E1 and PGT-PS-E3.

at 25.2°, 37.8°, 48.1°, 55.1°, 62.7°, 70.4°, respectively, corresponding to the (101), (004), (200), (105), (204) and (220) crystallographic planes of tetragonal TiO_2 in accordance with the synthetic anatase. When the oxygen-plasma treatment is up to 3 minutes, the diffraction peaks do not show significant change. No characteristic peaks belonging to other TiO_2 crystals or impurities were detected. The average anatase–TiO_2 particle size was approximately 3.2 nm, as estimated from the peak width of the anatase (101) reflection by using the Scherrer equation with a spherical model for approximation. Such a nanocrystalline pore-wall structure partially explains the stability of the nanostructure during the oxygen-plasma treatment. However, no diffraction peak can be attributed to GQDs in the WAXRD patterns. The reason may be attributed to the lower diffraction of intensity of GQDs in comparison with those of the characteristic peaks of TiO_2. For sample PGT-PS-E3, the weak and board peaks centered at 39.6° and 46.2° are attributed to the (111) and (200) reflections of Pt (JCPDF 01-1194) possessing a face-centered cubic structure with an *Fm3m* space group. And the peak at 43.2° can be identified as the reflection of the (004) lattice plane belonging to PtO_2 (JCPDS card no. 73-2360).[30] This means that the platinum element is present in several forms including metal (Pt) and tetravalent metal oxide (PtO_2) through oxygen-plasma treatment in the nanocomposite TiO_2 thin films. These peaks are weak and broad, indicating the nanocrystalline nature of the platinum particles encapsulated in the films. However, the peaks of PtO_2 are not observed in the pattern of PGT-PS-E1.

Fig. 3 shows PL spectra of PGT-PS-E1 (a), PGT-PS-E2 (b), PGT-PS-E3 (c), and PGT-PS-E4 (d). It can be seen that all the films show obvious PL signals with similar curve shape while the intensities are different. For the PL spectra of all the films, we could observe two peaks at around 418 nm and 438 nm. The peak ar the band of 418 nm is due to the surface recombination transition. Another peak at around 438 nm can be attributed to oxygen vacancies. Aluri *et al.* pointed out that the oxygen vacancy defects on the surface of TiO_2 are the 'active sites' for the adsorption of oxygen molecules. It has been observed that oxygen adsorption on TiO_2 surface quenches the PL intensity.[3] Because oxygen-plasma treatment forms more oxygen vacancies which could trap photoinduced electrons, the PL intensity of PtO_x/GQDs/TiO_2 composite film becomes lower with the increase of plasma treatment time. With the increase of oxygen-plasma treatment time, the nanocomposite film provides more trapping centers and promotes more electrons transferring from the valence band to the conduction band, and therefore suppresses the recombination of charge carriers more efficiently.[31] Rani *et al.* reported that the high PL intensity would result in a corresponding increment in hole density that dominates over the electron density at the film surface.[32] This would cause the p-type sensing behaviour of the PtO_x/GQDs/TiO_2 composite film. On the other hand, Wang *et al.* found that the PL of the PtO_x/GQDs/TiO_2 composite films is a representation of the ordering structure of sensing film.[24] The ordering structures lead to the intensity change of the integrated PL spectra for different oxygen-plasma treated films. The intensity change of the PL spectra of PtO_x/GQDs/TiO_2 suggests that it is highly likely a consequence of the formation of Ti–O–C bond as the formation of ordered nanostructure most likely takes place between the defects and oxygenated functional groups of GQDs and the surface of TiO_2 nanoparticles. This is also consistent with the fact that ordered nanostructures with the defects and oxygenated functional groups of GQDs are the chemically reactives sites with VOCs gas.

Specifically, the UV/Vis spectra of solid film of the synthesized GQDs has a strong absorption peak around 330 nm as a result of the π–π* transition of aromatic sp^2 domains,[33] and in contrast, the absorption in the visible range is low and flat as shown in Fig. S1.† The plain Pt–TiO_2 film (a) also has its absorption peak in the UV range as expected. After addition of GQDs, all PtO_x/GQDs/TiO_2 composite thin films (PGT-PS-E1 (b), PGT-PS-E2 (c), PGT-PS-E3 (d), and PGT-PS-E4 (e)) show enhanced absorption in the visible range in Fig. 4, the resulting composite absorb visible light by a quantum-confined bandgap narrowing mechanism and the results are listed in Table S1.† Such an improvement of visible light absorption is attributed to a quantum confined bandgap narrowing mechanism in which additional energy states formed below the conduction bands

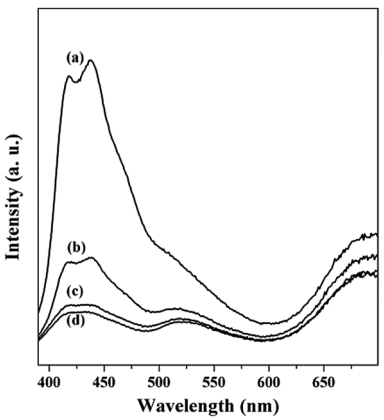

Fig. 3 PL spectra of (a) PGT-PS-E1, (b) PGT-PS-E2, (c) PGT-PS-E3, and (d) PGT-PS-E4.

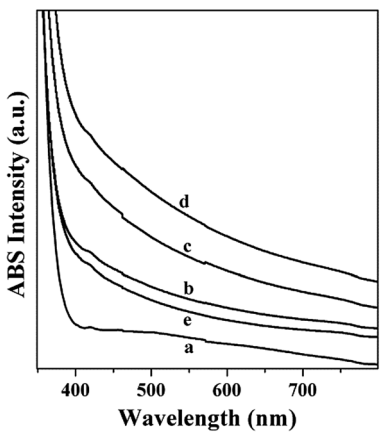

Fig. 4 UV-Vis spectra of (a) Pt–TiO_2 film, (b) PGT-PS-E1, (c) PGT-PS-E2, (d) PGT-PS-E3, and (e) PGT-PS-E4.

and above the valence bands of TiO_2 and GQDs due to the formation of Ti–O–C bond between GQDs and TiO_2 nanoparticles. The visible light absorption enhances monotonically from the PGT-PS-E1 to PGT-PS-E3 films, whereas the nanostructure ordering achieves the maximum in the PGT-PS-E3 film. The enhancement of visible absorption possesses an integrated trend with the ordering increase of nanostructure and the decrease of GQDs size and amount. Consequently, the UV-Vis spectra of visible light in this research show that: (1) the enhancement of visible light absorption can be achieved by modifying the interaction between GQDs and TiO_2 nanoparticles and the increase of nanostructure ordering under the oxygen-plasma treatment. (2) The decrease of GQDs size and amount induces the reduction of the visible light absorption by the oxygen-plasma treatment. Accordingly, the visible light absorption shows an oxygen-plasma treatment dependent feature that is the intensity of visible-light absorption is tardily up from PGT-PS-E1 to PGT-PS-E3. However, when the oxygen-plasma time is up to 4 minutes, the visible light absorption of PGT-PS-E4 with very little content of GQDs dramatically decreases. Clearly, oxygen-plasma treatment is able to make effective adjustment on the nanostructure ordering and quantum confined bandgap of sensing film, which plays a significant role in the improvement of sensing activity of PtO_x/GQDs/TiO_2 films.

The surface area and pore size distribution of PGT-PS-E1 and PGT-PS-E3 are analysed from nitrogen adsorption–desorption isotherms as shown in Fig. 5. In Fig. 5a, the N_2 adsorption–desorption isotherms for both samples show typical type IV curves with distinct condensation step at a p/p_0 range of 0.4–0.8. The calculated specific surface area and total pore volume of PGT-PS-E1 are observed as 122 $m^2\ g^{-1}$ and 0.31 $cm^3\ g^{-1}$, respectively. Its transformation into PGT-PS-E3 by further plasma oxygen treatment is accompanied by increase in the surface area and total pore volume up to 236 $m^2\ g^{-1}$ and 0.57 $cm^3\ g^{-1}$. Clearly, with the increase of the oxygen-plasma treatment time from 1 minute to 3 minutes, the template has been removed completely, and the thin film shows narrower pore width distribution confirming the highly ordered uniform pore structure (in Fig. 5b), in accord with the SAXRD results. As discussed above, for the PtO_x/GQDs/TiO_2 thin film, the oxygen-plasma treatment has an important effect on the nanostructure ordering, surface areas, and pore size distribution of the thin film. The thin film PGT-PS-E3 shows highest surface areas, big pore volume, excellent nanostructure ordering, and highest absorption in visible light region. In the following section, further discussion would be focus on the PGT-PS-E3 thin film.

The changes in morphology at the surface of the PtO_x/GQDs/TiO_2 thin films (PGT-PS-E1 and PGT-PS-E3) are compared in Fig. 6. Fig. 6a and b show the high magnification SEM images of the films obtained with the block copolymer (PGT-PS-E1) and after the further plasma treatment for 3 minutes (PGT-PS-E3), respectively. The surface of the film with the plasma treatment for 3 minutes is smooth (Fig. 6b). Both of these films with plasma treatment for different time show nanoporous structures with a regular pore system. The film (PGT-PS-E1) depicts a structure with small periodic domains, while the surface covered with large amount of block copolymer leads to less periodic structure on the film. Fig. 6b shows the SEM image of PtO_x/GQDs/TiO_2 thin film (PGT-PS-E3). Plasma treatment removes the polymer, leaving the TiO_2 framework with interconnecting spherical nanopores with an average diameter of about 5 nm, which is in accordance with the BET results. The nanopore size corresponds to the void space formed after removing the polymer. The film (PGT-PS-E3) exhibits the higher degree of periodicity and the larger size of periodic domains. In Fig. 6c and e (PGT-PS-E1) and Fig. 6d and f (PGT-PS-E3), elemental mapping analysis demonstrates the distribution of elements C and Pt, respectively. The C and Pt elemental maps illustrate an obvious concentrated distribution on the thin films. It appears that the sample PGT-PS-E1 presents larger amount of C element. However, the intensity of C in PGT-PS-E3 decreases significantly by further plasma oxygen treatment. For Pt element, the reduction of Pt content is not significantly obvious.

The TEM images of PGT-PS-E1 and PGT-PS-E3 are shown in Fig. 7. For the sample PGT-PS-E1 shown in Fig. 7a, there are many GQDs aggregates on the surface of thin film. From the SAED pattern (the inset image of Fig. 7a), it can be seen that the

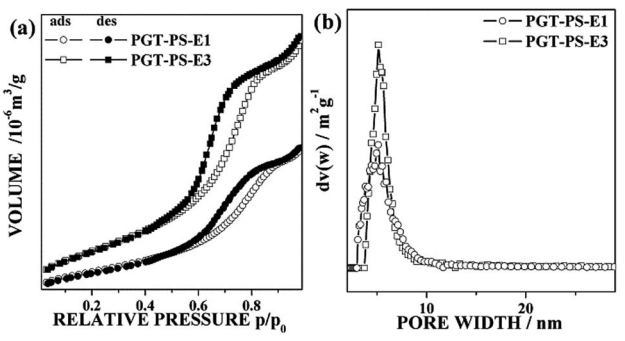

Fig. 5 (a) N_2 adsorption/desorption isotherms and (b) corresponding pore-size distribution for PGT-PS-E1 and PGT-PS-E3.

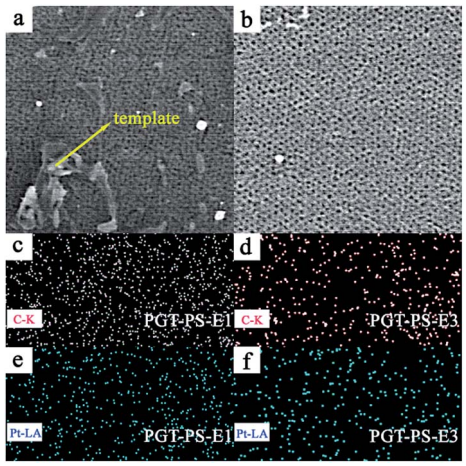

Fig. 6 (a) FESEM image of the PGT-PS-E1 sample; (b) FESEM image of the PGT-PS-E3; (c) and (e) EDX mapping analysis of PGT-PS-E1; (d) and (f) EDX mapping analysis of PGT-PS-E3.

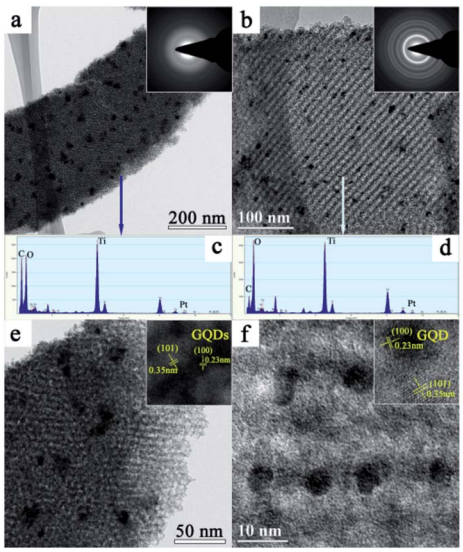

Fig. 7 (a) and (b) TEM image of PGT-PS-E1 and PGT-PS-E3, respectively. The inset is the SEAD pattern; (c) and (d) are EDX pattern of PGT-PS-E1 and PGT-PS-E3, respectively. (e) and (f) show high magnification images of PGT-PS-E1 and PGT-PS-E3. The inset shows HRTEM image of both samples.

crystallinity of the PGT-PS-E1 is not good, because the surface is covered with large number of GQDs aggregation. The further oxygen-plasma treatment from the thin film outer and inner surfaces leads to a remarkable decrease of GQDs aggregation in PGT-PS-E3 as shown in Fig. 7b, and the increase of oxygen-containing groups do play an important role in GQDs-support interactions. The good interaction between the GQDs and TiO_2 nanoparticles could efficiently minimize the electrical isolation of nanostructure during the gas sensing measurement. In the inset image of Fig. 7b, SAED pattern reveals well defined circular rings, suggesting the polycrystalline nature of PtO_x/GQDs/TiO_2 thin film. These rings could be indexed to the planes of anatase phase, which agrees well with the wide-angle XRD result above. The elemental analyses of the PtO_x/GQDs/TiO_2 thin film are obtained by energy-dispersive spectroscopy (EDS) for Ti, C, O, and Pt as shown in Fig. 7c and d. The EDS measurement confirms the existence of C, O, Ti and Pt elements in the both nanoporous sensing thin films. It is found that low temperature oxygen-plasma treatment leads to the decrease of carbon content from PGT-PS-E1 to PGT-PS-E3, the result is maybe small-sized GQDs coated on the surface of TiO_2 nanoparticles.

Fig. 7e and f show the high magnification and HRTEM image of PGT-PS-E1 and PGT-PS-E3, respectively. They possess the anatase phase, with a lattice spacing of 0.35 nm, which agrees well with the (101) planes of the anatase phase. The presence of the GQDs in the thin film was further confirmed by the HRTEM image, as displayed in the inset images of Fig. 7e and f. The high magnification HRTEM image shows the lattice spacing of 0.23 nm, corresponding to the (100) planes of graphitic carbon. As shown in Fig. 7f, the GQDs are found to be well dispersed on porous TiO_2 thin film with highly uniform size because of the presence of abundant functional groups. He *et al.* reported that the surface oxygen-containing groups on GQDs surfaces are initially important to enhance the loading and dispersion of Pt nanoparticles,[34] which is very important for PtO_x/GQDs/TiO_2 based VOCs sensor to obtain high sensitivity.

To get further insights in the chemical composition of thin film surface, PGT-PS-E1 and PGT-PS-E3 thin films are studied by XPS. The representative high-resolution XPS spectra comprising C 1s and Pt 4f are shown in Fig. 8. Fig. 8a displays the high-resolution spectra of the C 1s region of PGT-PS-E1 and PGT-PS-E3, respectively. The C 1s spectrum of the PGT-PS-E1 contains four components: the nonoxygenated ring C (284.7 eV), C–OH and C–O–C species (285.3 eV), C=O species (286.5 eV) and COOH species (288.6 eV). It is obviously observed that the peak of nonoxygenated ring C is much higher than that of C–OH and C–O–C species. While, in the C 1s spectrum of the sample PGT-PS-E3, the peak of C–OH and C–O–C species increase gradually which suggests that GQDs is heavily oxidized and holds more hydroxyl and epoxy groups. The enhancement of O-rich groups makes the GQDs provide additional advantages for further functionalization meeting sensing requirement. Moreover, GQDs play a leading role in revolution of the sensing devices owing to their potential in exceeding the Shockley–Queisser limit, their size-tuned optical response, and their efficient multiple carrier generation. Therefore, GQDs with high specific area, high mobility and tunable band gap should have great potential as electron-acceptors in sensing devices.

In Fig. 8b, the Pt 4f core level line of the PGT-PS-E1 sensing film could be fitted with two main doublets with E_b of Pt $4f_{7/2}$ at 70.9 eV and 72.3 eV. The platinum state with the lower E_b can be assigned to elemental Pt. The Pt $4f_{7/2}$ peak with the higher E_b could be assigned to Pt^{2+} in platinum oxide (PtO). Fig. 8b also presents the spectrum registered for the platinum 4f orbital of PGT-PS-E3 thin film, with deconvoluted peaks. On the basis of the fitting procedure there are distinguished three doublets of Pt $4f_{5/2}$ and Pt $4f_{7/2}$. Doublet a is assigned to Pt(0), b to Pt^{2+} in platinum oxide (PtO) and doublet c corresponds to Pt^{4+} in platinum dioxide (PtO_2). The atomic concentration of Pt oxidation states is different with regard to both examined samples. It should be noted that the presence of Pt^{4+} in platinum dioxide (PtO_2) is regarded as the oxidation state with higher activity than Pt(0) and Pt(II). The significant changes of surface composition and electronic interaction can greatly

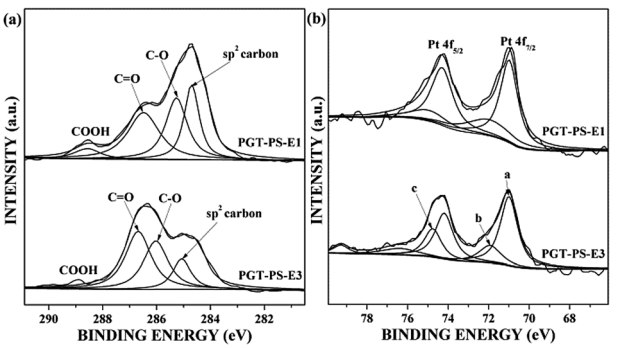

Fig. 8 (a) C 1s, and (b) Pt 4f spectra of PGT-PS-E1 and PGT-PS-E3.

influence the sensing behaviour of the PtO_x/GQDs/TiO_2 thin film. For sample PGT-PS-E1 with more GQDs aggregation and more content of Pt, PtO_x/GQDs composite quantum dots could increase the adsorption of oxygen molecules due to their spill-over effect. The adsorption of oxygen on the surface may focus on the PtO_x/GQDs layer, and will make more electrons be trapped, and then the depletion layer will be thicker, which will result in the forming of the inversion layer on the TiO_2 nanoparticles. Consequently, holes become the dominant carriers between PtO_x/GQDs layer and TiO_2 layer, and the conduction type of the thin films will be p-type. For sample PGT-PS-E3 under further oxygen-plasma treatment, GQDs show more oxygen functional groups, which is in favor of establishing more effective interaction between GQDs and TiO_2 nanoparticles. Kim *et al.* reported that the oxygen-rich functional group could favorably interacts with oxygen functional group in VOCs,[2] which could form an electron-rich region and causing charge transfer through the interface between GQDs and TiO_2 nanoparticles. On the other hand, oxygen-rich functional groups not only provides high energy binding sites for benzene but also interrupts direct binding of benzene onto the PtO_x/GQDs layer. Therefore, PtO_x/GQDs/TiO_2 thin films under different levels of oxygen-plasma treatment will present different sensing behaviour to VOCs gas.

3.2 Application to VOCs sensing

Owing to the solution processability of the PtO_x/GQDs/TiO_2 nanocomposite films, their sensor fabrication was conducted *via* the spin-coating method at room temperature, which was expected to bring about the benefits of nanostructure material in real sensors devices by overcoming the agglomeration issue encountered in high-temperature fabrication processing. As shown in Scheme 1, during the evaporation process, citric acid are likely to play an essential role tin the formation of the inorganic intermediate network (as shown in step a), as result of an ordered arrangement of graphene quantum dots. However, the whole synthetic system only with HCl could not present ordered arrangement of thin film after the evaporation process. Post-treatment of formed hybrid thin film by aging under controlled external humidity and temperature becomes a crucial step to obtain the crystalline nanostructure (in step b). It should be noted that the psHT treated nanocomposite films were capped with abundant surfactant, the long carbon chains of which hinder both the gas adsorption and carrier transport in the sensor device. We therefore applied an oxygen plasma treatment to remove most surfactant. Hence, anatase crystalline pore walls can be achieved at low temperature allowing an easy oxygen-plasma removal of the template without loss of nanoporous structure or significant shrinkage of the nanopore array normal to the sensor device substrate (step c and d). G. S. Aluri *et al.* fabricated TiO_2 based hybrid gas sensor depicted poor sensitivity to VOCs gas ar room temperature,[3] while our work presents the highly ordered PtO_x/GQDs/TiO_2 sensing films can be a good candidate to achieve room temperature gas sensing with excellent sensing performance.

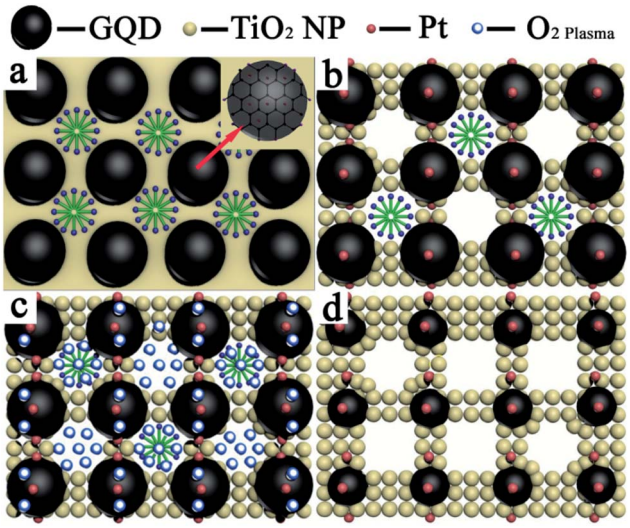

Scheme 1 Synthetic mechanism of PtO_x/GQDs/TiO_2 sensing film.

3.2.1 Sensing behavior to oxygen-functionalized VOCs. The sensing capability is experimentally tested by recording the change in the sensor's resistivity when the sensor is exposed to different concentrations of the target gas. The sensor response (S) is defined as $(R_a - R_g)/R_g$ or $=(R_a - R_g)/R_a$, where R_a and R_g are the sensor resistances in air and in the target gas, respectively. This parameter is positive (negative) for n-type (p-type) isopropanol sensing. Fig. 9a shows response curves of PtO_x/GQDs/TiO_2 nanocomposite films to the isopropanol gas at different concentrations ranging from 0.1 ppm to 40 ppm under 460 nm light illumination and the test are switched from low concentration to high concentration, and then conversely from high concentration to low concentration. At the beginning of testing, only dry air flows through the testing chamber to keep the baseline constant. When the chamber is exposed with isopropanol gas, the chamber is irradiated under a light with $\lambda =$ 460 nm at once. In the test, a constant electric field (2 V) and light intensity are used in all measurements. After 20 seconds of light irradiation, the light was turned off, and the response behaviour is continually monitored until it returns to the original level (this took ~30 seconds). The PtO_x/GQDs/TiO_2 gas sensor is then exposed to the same light irradiation again. An unusual but reversible behavior is instead observed when exposing different PtO_x/GQDs/TiO_2 nanocomposite sensing films to isopropanol gas under visible light illumination at room temperature. In Fig. 9a, we can find that the type of sensing response depends on the oxygen-plasma treatment time. The PtO_x/GQDs/TiO_2 gas sensors with less than 2 minutes oxygen-plasma treatment time show the reverse p-type sensing response with $S < 0$ to isopropanol gas. With increase plasma treatment time from 2 minutes to 3 minutes, the sensor switches to the n-type response with $S > 0$ and the response magnitude improves dramatically. The details are depicted in Fig. 9b. The response values (S) of different samples are −1.7 (PGT-PS-E1), −0.5 (PGT-PS-E2), 4.4 (PGT-PS-E3), and 2.3 (PGT-PS-E4), respectively. Typically, the response value of PGT-PS-E3 to 1 ppm isopropanol under light irradiation is 4.4, which is almost three times as that in the darkness (Fig. S2†).

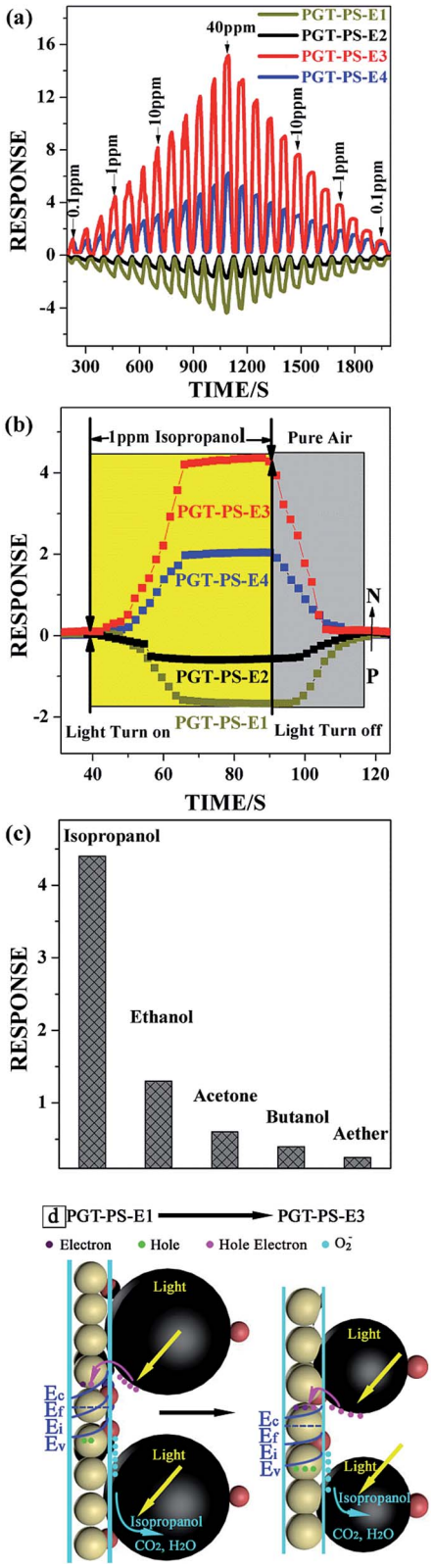

Fig. 9 (a) Response curves of different PtO_x/GQDs/TiO_2 films sensors measured under various isopropanol gas concentrations; (b) typical response and recovery curves of the different PtO_x/GQDs/TiO_2 film sensor to isopropanol gas at 1 ppm; (c) selectivity of PGT-PS-E3 to 1 ppm VOCs with oxygen functional group; (d) sensing mechanism of PGT-PS-E1 and PGT-PS-E3 to VOCs with oxygen functional group.

Selectivity is another significant property for the PtO_x/GQDs/TiO_2 based gas sensor, because poor selectivity will lead to mistaken alarm and hinder its massive utilization. Several vapour organic compounds with oxygen functional group are tested to probe into the potential application of PGT-PS-E3 as a remarkable sensor in terms of high sensitivity and fast response for 1 ppm concentration of chemical vapour detection at room temperature under visible light illumination. As shown in Fig. 9c, the PGT-PS-E3 based gas sensor displays quite outstanding selectivity to isopropanol, and the responses reach 4.4, 1.3, 0.6, 0.4, and 0.3 to isopropanol, ethanol, acetone, butanol, and aether, respectively.

3.2.2 Sensing mechanism of oxygen-functionalized VOCs response. For sample PGT-PS-E1, there is a sharp increase in the resistance of the sensing film when the isopropanol gas is pulled in the chamber. Subsequently, the resistance drops rapidly with exposure to air, which is p-sensing behaviour with $S < 0$. Due to more PtO_x/GQDs composite quantum dots being deposited on the surface of PGT-PS-E1 film, the isopropanol vapor reacts mainly at the PtO_x/GQDs/TiO_2 interface layer, and isopropanol incorporation into the PtO_x/GQDs layer could form shallow donors. The contributed electrons by isopropanol incorporation are migrated to the sensing films and are restricted by the PtO_x/GQDs layer. The band bends upward more dominantly, resulting in the formation of an inversion layer near the surface, where the intrinsic level (E_i) is above the Fermi level (E_f). In this inversion layer, hole is the majority carrier, which issues in a p-type sensing behaviour as shown in the left of Fig. 9d. With the further oxygen-plasma treatment, for sample PGT-PS-E3, GQDs show more oxygen functional groups and small size, which is in favor of establishing more effective interaction between GQDs and TiO_2 nanoparticles. It leads to the dramatical decrease of inversion layer thickness between GQDs and TiO_2 nanoparticles, where the Fermi level becomes higher than the intrinsic level as shown in the right of Fig. 9d. Furthermore, the PGT-PS-E3 thin film shows highest surface areas, big pore volume, excellent nanostructure ordering, and highest absorption in visible light region. Upon the visible light irritation, more excited electrons and positive holes are produced. Zheng *et al.* reported that[35] unlike the chemisorbed oxygen ions ($O_{2,ads}^-$), which are strongly attached to the TiO_2 nanoparticle surface, the visible light-induced oxygen ions ($O_{2,h\nu}^-$) are weakly bound to the TiO_2 nanoparticles, and they are highly reactive and responsible for the room-temperature gas sensitivity. Therefore, upon exposure to isopropanol gas, the photo-induced oxygen ions ($O_{2,h\nu}^-$) play a major role in the redox reaction at room temperature, leading to the enhancement of gas sensing performance greatly. On the other hand, the oxygen-rich functional group in GQDs could favorably interact with VOCs' oxygen functional group, which could form an electron-rich region, cause charge transfer through the interface between GQDs and TiO_2 nanoparticles quickly and enhance the response speed. It produces a depletion layer instead of the inversion layer, and the PtO_x/GQDs/TiO_2 sensing film shows n type sensing behaviour with $S > 0$.

3.2.3 Sensing behavior to aromatic VOCs. Fig. 10a presents response curves of PtO_x/GQDs/TiO_2 nanocomposite films to the

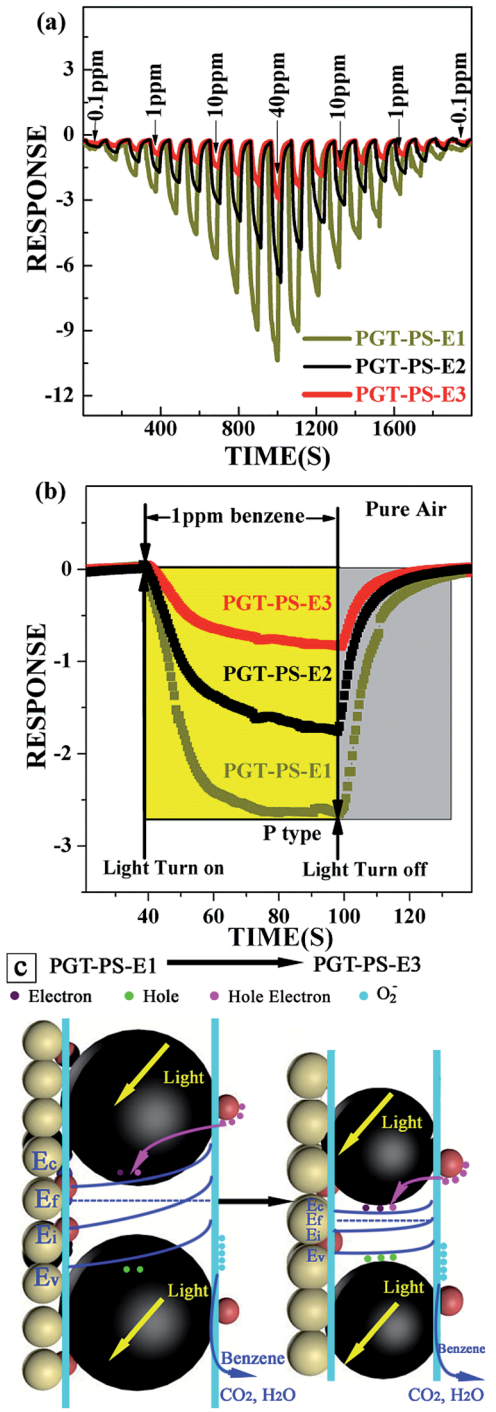

Fig. 10 (a) Response curves of different PtO_x/GQDs/TiO_2 films sensors measured under various benzene gas concentrations; (b) typical response and recovery curves of the different PtO_x/GQDs/TiO_2 film sensor to benzene gas at 1 ppm; (c) sensing mechanism of PGT-PS-E1 and PGT-PS-E3 to benzene.

benzene gas at different concentrations ranging from 0.1 ppm to 40 ppm under 460 nm light illumination. In our case, gas-sensing measurements are performed in dry air atmosphere to avoid any interference from humidity. p-Type sensing behaviour to benzene gas is observed for three PtO_x/GQDs/TiO_2 gas sensing films, we also find an increase in sensitivity with increasing gas concentration for all samples. However, the sensitivity of three samples decreases with the increase of oxygen-plasma treatment time at room temperature under the visible light illumination. The details of sensing response are shown in Fig. 10b, and $|S|$ of three samples to 1 ppm benzene are 2.6 (PGT-PS-E1), 1.7 (PGT-PS-E2), and 0.8 (PGT-PS-E3), respectively. These gas sensors present p-type sensing performance for benzene with different oxygen-plasma treatment. Without the addition of PtO_x, the GQDs/TiO_2 sensing film with 3 minutes oxygen-plasma treatment shows n-type sensing behaviour to benzene. However, the response value is only 0.1 to 1 ppm benzene as shown in Fig. S3.† Thus it can be seen that the PtO_x/GQDs heterojunction plays an important role in tuning the sensing performance of the composite film.

3.2.4 Sensing mechanism of aromatic VOCs response. The sensing mechanism of benzene response is shown in Fig. 10c. Meng *et al.*[36] reported that the plane structure and the π-conjugate system of the benzene molecule make itself strong adsorb on the surface of the graphene quantum dots. So, benzene has a higher heat of adsorption on PtO_x/GQDs layer than on PtO_x/TiO_2 layer. Thus, benzene will preferentially adsorb on PtO_x in the PtO_x/GQDs layer. In the PtO_x/GQDs heterojunction, the work function of PtO_x (~5.6 eV) is larger than that of GQDs (~4.75 eV). In order to align the Fermi level, the electrons will flow from GQDs to PtO_x sides, as the electrostatic potential of the GQDs is increased. The Schottky barriers (0.85 eV) generated at PtO_x/GQDs heterojunctions will provide high modulation of resistance during the adsorption and desorption of benzene by changing the heterojunction barrier. For sample PGT-PS-E1, there are numerous PtO_x/GQDs composite quantum dots on its surface, where the intrinsic level (E_i) is much higher than the Fermi level (E_f), as shown in the left of Fig. 10c. It results in the higher and faster p-type sensing response to sub-ppm concentration of benzene than other two samples. For sample PGT-PS-E3, with further oxygen-plasma treatment, more oxygen functional groups, especially carbonyl groups, are formed on the GQDs as shown in XPS results. The oxygen-rich functional groups not only provide high energy binding sites for benzene[2] but also interrupt direct binding of benzene onto the PtO_x/GQDs layer. On the other hand, the carbonyl groups have dominant effect on increasing the work function value of GQDs.[37] It results in the decrease of Schottky barriers generated at PtO_x/GQDs heterojunctions, and leading to the lowering of the position of the intrinsic level (E_i), but it remains above the Fermi level as shown in the right of Fig. 10c. Therefore, PGT-PS-E3 sensor still shows p type sensing performance to benzene gas with lower response value.

4. Conclusions

In summary, we demonstrates a tunable volatile organic compounds sensing behavior under visible light illumination obtained by applying PtO_x/GQDs decorated TiO_2 thin film at room temperature, which is synthesized *in situ* on a sensing device using water vapor hydrothermal treatment and oxygen-plasma treatment. The structure, crystallinity and composition of the ordered nanoporous PtO_x/GQDs/TiO_2 thin films are

characterized by HRTEM, FESEM, SAED, and XPS. The sensing properties of PtO_x/GQDs/TiO_2 thin film sensors are investigated by exposing it to VOCs gas with a concentration range from 0.1 ppm to 40 ppm under visible light illumination. Interestingly, the PtO_x/GQDs/TiO_2 nanocomposite thin films depict reversible change of sensing behaviour from p-type to n-type sensing behaviour for oxygen-functionalized VOCs as function of oxygen-plasma treatment, while these gas sensors present p-type sensing performance for aromatic VOCs throughout. Furthermore, these gas sensors exhibit high sensitivity to isopropanol gas with response value up to 4.4 to 1 ppm and a short response time of 9 second at room temperature. This synthesis procedure to fabricate a tunable and sensitive VOCs sensor may lead to a potential real-world application for breath diagnosis.

Conflicts of interest

There are no conflicts to declare.

Acknowledgements

This work was supported by the Startup Foundation for Introducing Talent of NUIST (2014r034), Project of Natural Science Research in University of Jiangsu Province (17KJB430024), and Horizontal Subject (2016h036).

References

1 B. Buszewski, A. Ulanowska, T. Ligor, N. Denderz and A. Amann, *Biomed. Chromatogr.*, 2009, **23**, 551.
2 J. S. Kim, H. W. Yoo, H. O. Choi and H. T. Jung, *Nano Lett.*, 2014, **14**, 5941.
3 G. S. Aluri, A. Motayed, A. V. Davydov, V. P. Oleshko, K. A. Bertness, N. A. Sanford and R. V. Mulpuri, *Nanotechnology*, 2012, **23**, 175501.
4 J. Zhang, X. Liu, G. Neri and N. Pinna, *Adv. Mater.*, 2015, **28**, 795.
5 Y. Yang, Y. Liang, G. Wang, L. Liu, C. Yuan, T. Yu, Q. Li, F. Zeng and G. Gu, *ACS Appl. Mater. Interfaces*, 2015, **7**, 24902.
6 T. J. Wong, F. J. Lim, M. Gao, G. H. Lee and G. W. Ho, *Catal. Sci. Technol.*, 2013, **3**, 1086.
7 W. L. Ong, M. Gao and G. W. Ho, *Nanoscale*, 2013, **5**, 11283.
8 M.-H. Seo, M. Yuasa, T. Kida, J.-S. Huh, N. Yamazoe and K. Shimanoe, *Sens. Actuators, B*, 2011, **154**, 251.
9 D. H. Kim, Y.-S. Shim, H. G. Moon, H. J. Chang, D. Su, S. Y. Kim, J.-S. Kim, B. K. Ju, S.-J. Yoon and H. W. Jang, *J. Phys. Chem. C*, 2013, **117**, 17824.
10 E. Şennik, U. Soysal and Z. Z. Öztürk, *Sens. Actuators, B*, 2014, **199**, 424.
11 T. Plecenik, M. Moško, A. A. Haidry, P. Ďurina, M. Truchlý, B. Grančič, M. Gregor, T. Roch, L. Satrapinskyy, A. Mošková, M. Mikula, P. Kúš and A. Plecenik, *Sens. Actuators, B*, 2015, **207**, 351.
12 C.-H. Han, D.-W. Hong, S.-D. Han, J. Gwak and K. C. Singh, *Sens. Actuators, B*, 2007, **125**, 224.
13 L. Peng, Q. Zhao, D. Wang, J. Zhai, P. Wang, S. Pang and T. Xie, *Sens. Actuators, B*, 2009, **136**, 80.
14 H. Chen, Y. Liu, C. Xie, J. Wu, D. Zeng and Y. Liao, *Ceram. Int.*, 2012, **38**, 503.
15 J. Zhai, D. Wang, L. Peng, Y. Lin, X. Li and T. Xie, *Sens. Actuators, B*, 2010, **147**, 234.
16 I. S. Cho, C. H. Lee, Y. Feng, M. Logar, P. M. Rao, L. Cai, D. R. Kim, R. Sinclair and X. Zheng, *Nat. Commun.*, 2013, **4**, 1723.
17 W. Wang, Y. Zhou, Y. Wen, Y. Ni, C. Lu and Z. Xu, *Mater. Lett.*, 2015, **158**, 29.
18 J. Hensel, G. Wang, Y. Li and J. Z. Zhang, *Nano Lett.*, 2010, **10**, 478.
19 W. Wang, J. Fang, Y. Zhou, W. Zhang and C. Lu, *RSC Adv.*, 2016, **6**, 67556.
20 T. Zhu, W. Li Ong, L. Zhu and G. Wei Ho, *Sci. Rep.*, 2015, **5**, 10601.
21 W.-Y. Yan, Q. Zhou, X. Chen, X.-J. Huang and Y.-C. Wu, *Sens. Actuators, B*, 2016, **230**, 761.
22 L. Zhu, C. F. Tan, M. Gao and G. W. Ho, *Adv. Mater.*, 2015, **27**, 7713.
23 D. Pan, J. Jiao, Z. Li, Y. Guo, C. Feng, Y. Liu, L. Wang and M. Wu, *ACS Sustainable Chem. Eng.*, 2015, **3**, 2405.
24 S. Wang, I. S. Cole and Q. Li, *Chem. Commun.*, 2016, **52**, 9208.
25 S. Zhu, J. Zhang, X. Liu, B. Li, X. Wang, S. Tang, Q. Meng, Y. Li, C. Shi, R. Hu and B. Yang, *RSC Adv.*, 2012, **2**, 2717.
26 X. Wang, H. Bai and G. Shi, *J. Am. Chem. Soc.*, 2011, **133**, 6338.
27 Q. Yuan, A.-X. Yin, C. Luo, L.-D. Sun, Y.-W. Zhang, W.-T. Duan, H.-C. Liu and C.-H. Yan, *J. Am. Chem. Soc.*, 2008, **130**, 3465.
28 L. Robben, A. A. Ismail, S. J. Lohmeier, A. Feldhoff, D. W. Bahnemann and J.-C. Buhl, *Chem. Mater.*, 2012, **24**, 1268.
29 R. Liu, Y. Ren, Y. Shi, F. Zhang, L. Zhang, B. Tu and D. Zhao, *Chem. Mater.*, 2008, **20**, 1140.
30 X. Liu, N. Chen, B. Han, X. Xiao, G. Chen, I. Djerdj and Y. Wang, *Nanoscale*, 2015, **7**, 14872.
31 P. Zhang, X. Li, X. Wu, T. Zhao and L. Wen, *J. Alloys Compd.*, 2016, **673**, 405.
32 S. Rani, M. C. Bhatnagar, S. C. Roy, N. K. Puri and D. Kanjilal, *Sens. Actuators, B*, 2008, **135**, 35.
33 V. Gupta, N. Chaudhary, R. Srivastava, G. D. Sharma, R. Bhardwaj and S. Chand, *J. Am. Chem. Soc.*, 2011, **133**, 9960.
34 D. He, K. Cheng, T. Peng, X. Sun, M. Pan and S. Mu, *J. Mater. Chem.*, 2012, **22**, 21298.
35 Z. Q. Zheng, B. Wang, J. D. Yao and G. W. Yang, *J. Mater. Chem. C*, 2015, **3**, 7067.
36 F. L. Meng, H. H. Li, L. T. Kong, J. Y. Liu, Z. Jin, W. Li, Y. Jia, J. H. Liu and X. J. Huang, *Anal. Chim. Acta*, 2012, **736**, 100.
37 P. V. Kumar, M. Bernardi and J. C. Grossman, *ACS Nano*, 2013, **7**, 1638.

